Microstructure modelling of laser metal powder directed energy deposition of alloy 718

Citation for the original published paper (version of record):
Kumara, C., Segerstark, A., Hanning, F. et al (2019). Microstructure modelling of laser metal powder directed energy deposition of alloy 718. Additive Manufacturing, 25: 357-364.
http://dx.doi.org/10.1016/j.addma.2018.11.024

Additive Manufacturing 25 (2019) 357–364

Contents lists available at ScienceDirect

Additive Manufacturing

journal homepage: www.elsevier.com/locate/addma

Full Length Article

Microstructure modelling of laser metal powder directed energy deposition of alloy 718

Chamara Kumara[a,*], Andreas Segerstark[b], Fabian Hanning[c], Nikhil Dixit[a], Shrikant Joshi[a], Johan Moverare[a,d], Per Nylén[a]

[a] Division of Subtractive and Additive Manufacturing Processes, Department of Engineering Science, University West, 461 86 Trollhättan, Sweden
[b] GKN Aerospace Engine Systems AB, Trollhättan, SE-461 81, Sweden
[c] Department of Industrial and Materials Science, Chalmers University of Technology, 412 96 Gothenburg, Sweden
[d] Division of Engineering Materials, Department of Management and Engineering, Linköping University, SE-58183 Linköping, Sweden

ARTICLE INFO

Keywords:
Phase-field
DED
Heat treatment
Thermal cycle
Modelling

ABSTRACT

A multi-component and multi-phase-field modelling approach, combined with transformation kinetics modelling, was used to model microstructure evolution during laser metal powder directed energy deposition of Alloy 718 and subsequent heat treatments. Experimental temperature measurements were utilised to predict microstructural evolution during successive addition of layers. Segregation of alloying elements as well as formation of Laves and δ phase was specifically modelled. The predicted elemental concentrations were then used in transformation kinetics to estimate changes in Continuous Cooling Transformation (CCT) and Time Temperature Transformation (TTT) diagrams for Alloy 718. Modelling results showed good agreement with experimentally observed phase evolution within the microstructure. The results indicate that the approach can be a valuable tool, both for improving process understanding and for process development including subsequent heat treatment.

1. Introduction

Nickel-based superalloys represent one of the most important categories of alloys used in aerospace and gas turbine engines due to the desirable combination of good high-temperature strength, high resistance to creep deformation and corrosion resistance [1,2] that they offer. Among these superalloys, Alloy 718 is one of the most commonly employed nickel-iron based superalloys. This alloy has good weldability due to the sluggish precipitation of strengthening phases present in it [3]. Alloy 718 has a microstructure that is dominated by a γ Face Centred Cubic (FCC) matrix. Within the matrix, precipitates such as Laves, γ'/γ" (strengthening phases), δ and various metallic carbides and nitrides can be found [4]. The specific microstructure (phase constitution, phase distribution and morphology) of the alloy is mainly governed by the primary manufacturing technology and succeeding post-processing conditions. Suitable heat treatments are commonly employed to tailor the microstructure of Alloy 718 to achieve the properties required for any targeted application.

According to the ASTM standard [5] directed energy deposition (DED) process is an additive manufacturing process in which a focused energy source (eg: laser, electron beam, plasma arc) is used to fuse materials by melting as they are being deposited. The deposition material can be in the form of powder or wire [6]. In the present study, a laser source was used as the focused energy source and deposition material was in the form of powder. Thus in this article, this process is being referred to as laser metal powder directed energy deposition (LMPDED). Among the repair methods for worn and corroded gas turbine components, this LMPDED method has become popular due to that fact that the parts can be repaired with minimal dilution and distortion [7]. In addition, this method is also used to add features to cast and forged components [8]. In layer-by-layer material deposition that LMPDED involves, the deposited material undergoes repeated heating and cooling when successive layers are being deposited. This causes the solidified material to experience remelting, resolidification and solid-state phase transformation, depending on the nature of the local thermal conditions (such as heating rates, cooling rates, thermal gradients, maximum temperature and number of thermal cycles). Prior published literature reveals that each of the above ultimately influence the underlying microstructure and the resulting mechanical properties [7,9–13].

Tian et al [7] reported a higher hardness in the bottom region than in the top region of Alloy 718 builds deposited by LMPDED. This was

* Corresponding author.
E-mail address: chamara.kumara@hv.se (C. Kumara).

https://doi.org/10.1016/j.addma.2018.11.024
Received 29 August 2018; Received in revised form 20 November 2018; Accepted 20 November 2018
Available online 22 November 2018

rationalised based on the measured thermal profiles at the bottom of the sample and the niobium (Nb) segregation during thermal cycles. The above finding is consistent with the observations made by Zhang et al. [12] and Tabernero et al. [14] in as-built Alloy 718 samples fabricated using a similar process. Qi et al [10] studied the tensile properties of LMPDED Alloy 718 samples in the as-deposited condition and after standard heat treatments (direct age, solution treatment and age i.e., STA, and homogenization followed by STA). The observed differences in mechanical properties in as-built and post-treated conditions were correlated to the corresponding changes observed in microstructure. Liu et al [9] investigated the influence of two different laser scanning paths, namely single direction raster scanning (SDRS) and cross direction raster scanning (CDRS), on the microstructure and mechanical properties. The growth of columnar dendrites was observed to occur along the deposition direction in SDRS samples compared to CDRS samples. However, the CDRS samples showed better ductility compared to the SDRS samples. Apart from experimental studies, modelling studies have also been performed on LMPDED, with the primary focus being on predicting melt pool characteristics, thermal conditions, grain structure and residual stresses [8]. However, relatively less attention has been paid to developing models to predict microconstituent phase formation during the LMPDED process. Nie et al [15] showed the presence of relationships between cooling rates as well as thermal gradients and Laves phase formation during LMPDED of Alloy 718 through stochastic modelling work using a simplified nickel (Ni)-niobium (Nb) Alloy system. Their observations indicated that low thermal gradients and high cooling rates can lead to a distribution of Laves phase as discrete particles rather than in the form of a continuous network and, thus, reduce the risk of cracking.

Based on the above, it is apparent that an improved understanding of microstructure formation during the LMPDED process is important in order to achieve the desired build performance and quality. However, experimental observation of microstructure formation during the build process and subsequent post heat treatments is a difficult and time-consuming task. Therefore, reliable computational modelling methods are highly desirable for this purpose. In the present study, phase-field modelling, combined with transformation kinetics calculations, have been utilised to investigate microstructure formation (growth of dendrites, element segregation and phase formation) during LMPDED of Alloy 718 and subsequent heat treatment.

2. Experimental work

Gas atomized Alloy 718 powder was utilised to generate the LMPDED built samples in this study. The powder was deposited onto an as-cast Alloy 718 substrate using a coaxial nozzle equipped with a 6 kW Ytterbium fibre laser. The nozzle set-up was mounted on an IRB-4400 ABB Robot, which was used to control the motion during deposition of the Alloy 718 samples. Single-wall samples comprised of a single layer, 2-layers, 3-layers and 15-layers in the build direction were deposited. The width of the single wall was equal to a width of a single-track (~1.89 mm) and the length of the walls were roughly 35 mm. Table 1 shows the nominal compositions of both powder and substrate. The particle size of the powder was in the range of 20–75 µm. A volumetric powder feeding system was utilised to deliver the powder to the coaxial nozzle with an angular outlet. Argon was used as the carrier gas as well as the shielding gas. Table 2 shows the process parameters used in the present study to generate the deposits. Temperature measurements that served as input for the modelling work in this study were made at the first deposited track level, using type-K thermocouples according to the method previously described by Segerstark et al. [16].

The heat treatment performed in this study was according to the suggestion by Barron [17] and comprised solutionizing the sample using an air furnace at 954 °C/1 h - air-cooled followed by ageing at 760 °C/5 h-furnace cooled + 650 °C/1 h – air-cooled. This heat treatment is generally used in case of Alloy 718 repaired jet engine components to avoid coarsening of γ″ precipitates present in the base component.

Table 1
Nominal chemical composition of the raw powder and the nominal chemical composition used for the phase-field simulation. Substrate chemical composition is also given for the reference.

Element	Substrate (wt%)	Powder (wt%)	Simulation (wt%)
Fe	Bal.	Bal.	Bal.
Ni	53.4	52.7	52.7
Cr	18.35	17.5	17.5
Nb	5.24	5.0	5.0
Mo	3.02	3.17	3.17
Ti	0.92	1.07	1.07
Al	0.48	0.68	0.68
Co	0.08	0.2	–
Mn	0.04	0.065	–
Ta	–	0.003	–
Si	0.08	0.088	–
Cu	0.02	0.048	–
C	0.046	0.031	–
P	0.009	0.006	–
B	–	0.003	–

Table 2
LMPDED Process parameters used in this study.

Parameter	Value
Laser Power (W)	1000
Scanning Speed (mm/s)	10
Powder Feed rate (g/min)	10
Powder standoff distance (mm)	−1
Shielding gas flow rate (l/min)	11.5
Carrier gas flow rate (l/min)	3.2
Lase spot diameter (mm)	1.6

Table 3
Summery of the model parameters used in the multiphase-field simulations in MICRESS.

Parameter	Value
Domain size	25 µm × 20 µm
Grid resolution (Δx)	0.05 µm
Interface thickness (η)	2.5 ·Δx
Thermal Gradient	0
Interface Energy - Liquid/γ (J/cm^2)	1.2E-05 [33]
Interface Energy Liquid/Laves (J/cm^2)	6E-06
Interface Energy γ/Laves (J/cm^2)	5E-06
Interface Energy δ/γ (J/cm^2)	1E-05 [34]
Interface Energy δ/Laves (J/cm^2)	5E-06
Interfacial stiffness Coefficient - Liquid/γ	0.2
Interfacial mobility Coefficient - Liquid/γ	0.2
Interfacial stiffness Coefficient - δ/γ	0.05
Interfacial mobility Coefficient - δ /γ	0.05
Elongation factor for δ/γ Interfacial stiffness	2
Elongation factor for δ/γ interface mobility	0.02

For microstructure evaluation, samples were sectioned and mounted using non-conductive Bakelite. Zeiss EVO 50 Scanning Electron Microscope (SEM) was utilised to analyse the microstructure. In order to quantify the area fractions of Nb-rich constituents, SEM images were analysed using the open source software ImageJ. Microhardness measurements were performed using a Vickers micro-hardness testing machine with a load of 0.5 N and a dwell time of 10 s.

3. Modelling work

3.1. About MICRESS and the governing equations

The phase-field method has been utilized in the current work to

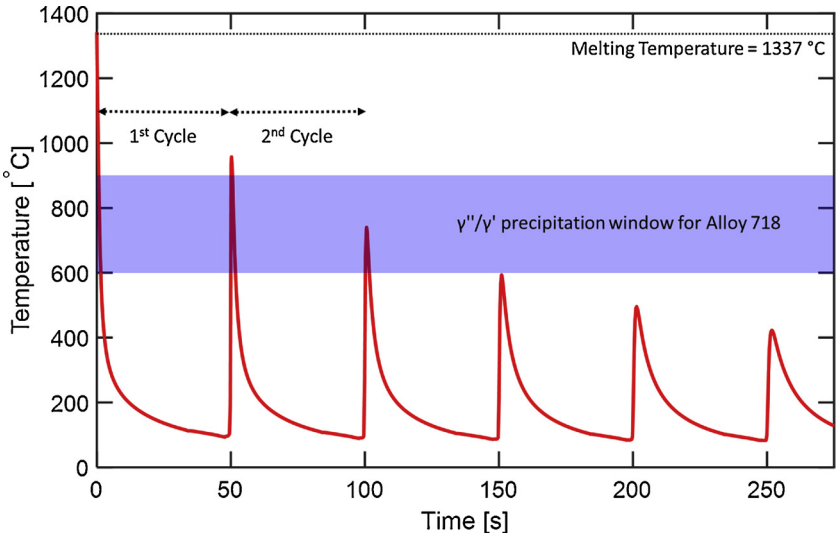

Fig. 1. Time-Temperature history measured at the 1 st deposited layer. Indicated precipitation windows for γ'/γ" for Alloy 718 was taken from [4] and the melting temperature was taken from Thermo-Calc calculation for reduced composition used in the MICRESS simulations.

model the evolution of microstructure during LMPDED and subsequent heat treatment. This method has been widely used to simulate microstructure evolution in materials in the past two decades [18,19]. The advantage of the phase-field method is that there is no need to track the interface, as in classical sharp interface modelling methods. This is achieved by introducing a phase-field parameter (also known as order parameter) that varies smoothly between two phases. Therefore, in the phase-field method, the interface will be a part of the solution.

The simulations in the current work have been performed using the commercially available phase-field software MICRESS (version 6.400, Access e.V., Aachen, Germany) based on the multi-phase-field approach [20,21]. The multi-phase-field theory describes the evolution of multiple phase-field parameters, $\phi_{\alpha=1,2,\ldots,v} = (\vec{x}, t)$, in space and time. These represent the spatial distribution of multiple phases with different thermodynamic properties and/or multiple grains with different orientations. The phase-field parameter, ϕ_α, assumes a value of 1 if the phase α is present locally and a value of 0 if the phase is not present locally. At the interface of the phase α, ϕ_α varies smoothly between 0–1 over the interface thickness of η. Only a summary of the formulation of the time evolution equations implemented in MICRESS software are presented here. A more detailed formulation is further described in [21,22].

The time evolution of the phase-field variable, ϕ_α, is calculated from the free energy functional F, which integrates the density functional f over the domain Ω.

$$F(\{\phi_\alpha\}, \{\vec{C}_\alpha\}) = \int_\Omega f(\{\phi_\alpha\}, \{\vec{C}_\alpha\}) \tag{1}$$

Here, the brackets {} contains all phases of α present in the domain, and should not be considered as a locally present α. $\vec{C}_\alpha$ represents the composition of the phase α. The density functional f depends on the interface energy density f^{int} and chemical free energy f^{chem} and can, therefore, be written as follows:

$$f = f^{int}\{\phi_\alpha\} + f^{chem}\{\{\phi_\alpha\}, \{\vec{C}_\alpha\}\} \tag{2}$$

$$f = \sum_{\alpha=1}^{v}\sum_{\beta\neq\alpha}^{v}\frac{4\sigma_{\alpha\beta}}{v\eta}\left(-\frac{\eta^2}{\pi^2}\nabla\phi_\alpha\nabla\phi_\beta + \phi_\alpha\phi_\beta\right) + \sum_{\alpha=1}^{v}\phi_\alpha f_\alpha(\vec{C}_\alpha) \tag{3}$$

In the Eq. (3) above, $\sigma_{\alpha\beta}$ represents the anisotropic interface energy of the interface between α and β. The variable v represents the total number of local co-existing phases. The multiphase-field equation, which defines the time evolution of $\phi_\alpha = (\vec{x}, t)$ in multiple phase transformations, is derived by minimization of the total free energy F following a relaxation principle.

$$\dot{\phi}_\alpha = -\sum_{\beta=1}^{v} M_{\alpha\beta}\frac{\pi^2}{8\eta}\left(\frac{\delta F}{\delta\phi_\alpha} - \frac{\delta F}{\delta\phi_\beta}\right) \tag{4}$$

A generic version of the multiphase-field equation can be written as [22]:

$$\dot{\phi}_\alpha = \sum_{\beta\neq\alpha}^{v} M_{\alpha\beta}\left[\frac{\sigma_{\alpha\beta}}{v}K_{\alpha\beta} + \sum_{\gamma\neq\beta\neq\alpha}^{n} J_{\alpha\beta\gamma} + |\nabla\phi|\,\Delta G_{\alpha\beta}\right] \tag{5}$$

$$K_{\alpha\beta} = \frac{1}{2}(\nabla^2\phi_\alpha - \nabla^2\phi_\beta) + \frac{\pi^2}{2\eta_{\alpha\beta}^2}(\phi_\alpha - \phi_\beta) \tag{6}$$

$$J_{\alpha\beta\gamma} = \frac{1}{2}(\sigma_{\beta\gamma} - \sigma_{\alpha\gamma})\left(\frac{\pi^2}{\eta^2}\phi_\gamma + \nabla^2\phi_\gamma\right) \tag{7}$$

Here, $M_{\alpha\beta}$ is the mobility of the α-β interface. The parameter $K_{\alpha\beta}$ is related to the local curvature of the interface. The interface motion depends on the curvature contribution ($\sigma_{\alpha\beta}K_{\alpha\beta}$) as well as on the thermodynamic driving force $\Delta G_{\alpha\beta}(\vec{C}, T)$. This driving force, in turn, depends on the temperature T and the local multi-component composition $\vec{C}$. The multi component composition couples the phase-field equation to the multi-phase diffusion equations given below.

$$\dot{\vec{C}} = \nabla\sum_{\alpha=1}^{v}\phi_\alpha\vec{D}_\alpha\nabla\vec{C}_\alpha \tag{8}$$

$$\vec{C} = \sum_{\alpha=1}^{v}\phi_\alpha\vec{C}_\alpha \tag{9}$$

The parameter $\vec{D}_\alpha$ in Eq. (7) represents the multi-component diffusion coefficient matrix for phase α. Here $\vec{D}_\alpha$ and $\Delta G_{\alpha\beta}(\vec{C}, T)$ are calculated through direct coupling to mobility and thermodynamic databases, respectively, via the TQ-interface of Thermo-Calc Software [23].

3.2. Model setup in MICRESS

In the present work, 2D simulations were carried out. The 2D domain was selected normal to the build direction in the 1st track of the LMPDED sample. Therefore, the domain is an isothermal section without any thermal gradients. In such a domain, the solidification simulations can be carried out by giving only a time-temperature history

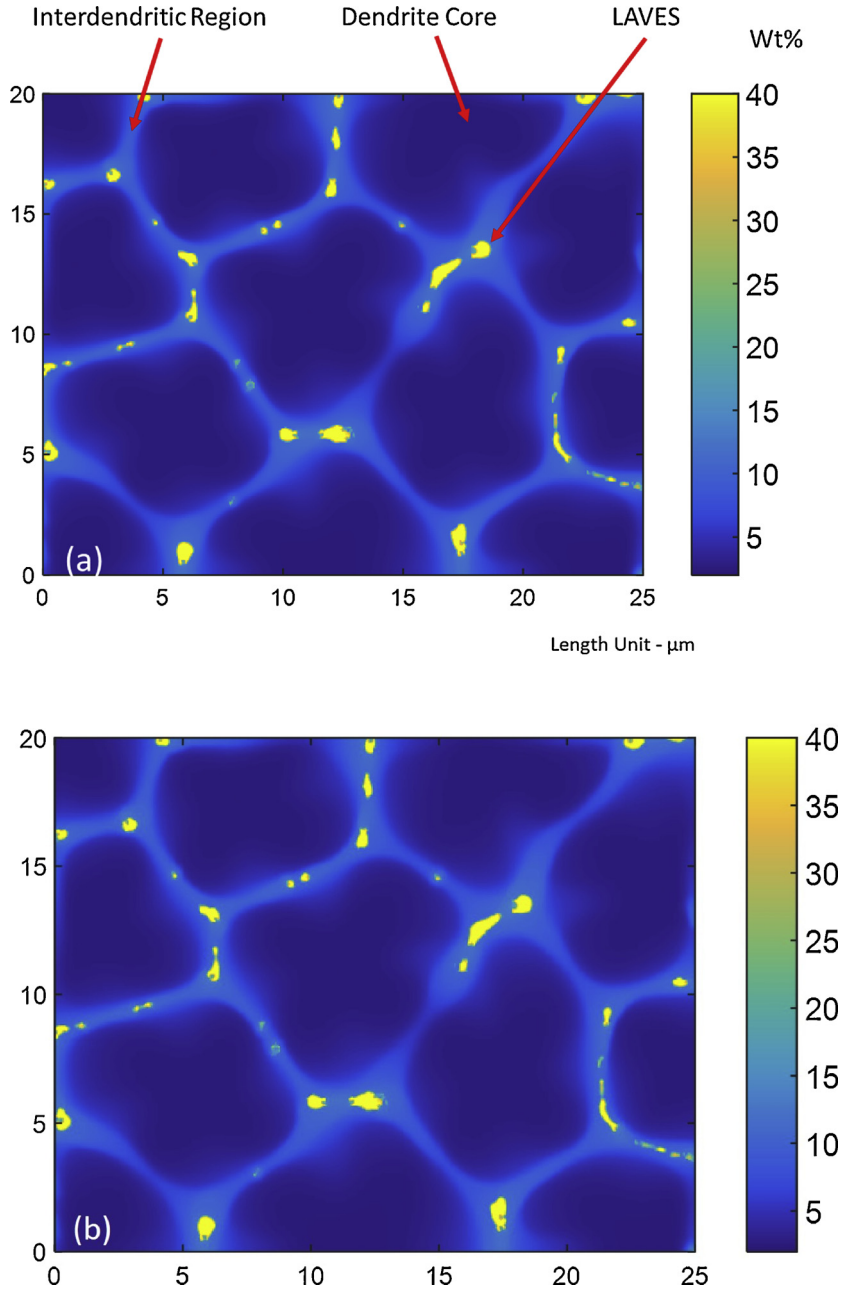

Fig. 2. Nb (wt%) distribution map (a) after the 1 st thermal cycle and (b) after the 2nd thermal cycle of the MICRESS simulations of the LMPDED process.

for the thermal conditions. A simulation domain size of 25 µm X 20 µm with 0.05 µm grid spacing was considered. Alloy 718 was modelled as a 7-component system having the composition shown in Table 4. This simplification was made to reduce the computational effort that is needed when calculating the thermodynamic and mobility data needed for the simulation. The thermodynamic and mobility data for the model was dynamically taken from TCNI8 and MOBNI4 databases from Thermo-Calc. In addition, a complete multicomponent diffusion matrix based on the local composition values was taken into account.

The simulations started from a complete liquid state, with the composition given in Table 4. 9 initial γ seeds were positioned in the domain such that the distance between seeds was roughly equal to the experimentally measured Primary Dendrite Arm Spacing (PDAS) of 7.1 µm. The initial temperature of the simulation was set to 1337 °C. This liquidus temperature value is taken from Thermo-Calc equilibrium calculations for the current alloy composition. The experimentally measured temperature profile in the 1st track served as input for the model as the thermal condition.

During solidification, phases such as titanium nitride (TiN), MC and Laves are known to form from the liquid [24]. However, TiN formation is not plausible in case of the nominal alloy composition considered in this study since it does not contain any nitrogen (N). In addition, MC too could not be modelled since the simplified alloy system does not contain carbon (C). γ' /γ" formation was also not modelled in the present work as, in order to capture the formation of these nano-scale precipitates, a very small grid spacing (typically in the rage of 1 nm) is required demanding greater computational effort. Hence, in the current phase-field modelling work, only formation of the Laves phase and δ phase were modelled to reduce the complexity of the model and associated computational effort.

During the simulation of microstructure evolution in LMPDED process, the Laves phase was allowed to nucleate at the liquid-γ interface. To simulate the eutectic formation of Laves + γ, nucleation site for eutectic γ was allowed to form at the liquid-Laves interface. For both

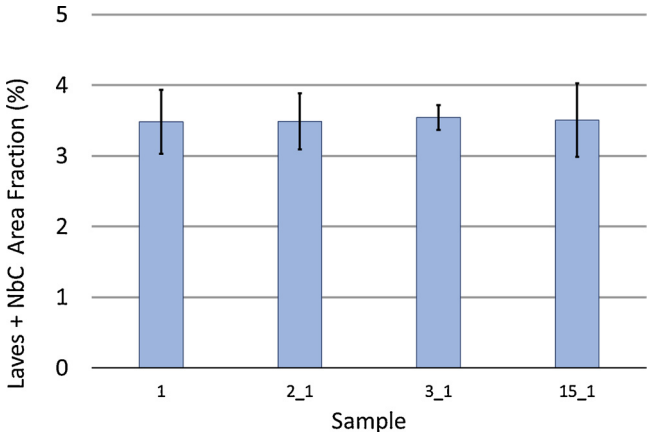

Fig. 3. Laves + NbC area fraction in the 1st layer of the deposited samples, with varying number of total deposited layers in the single wall samples.

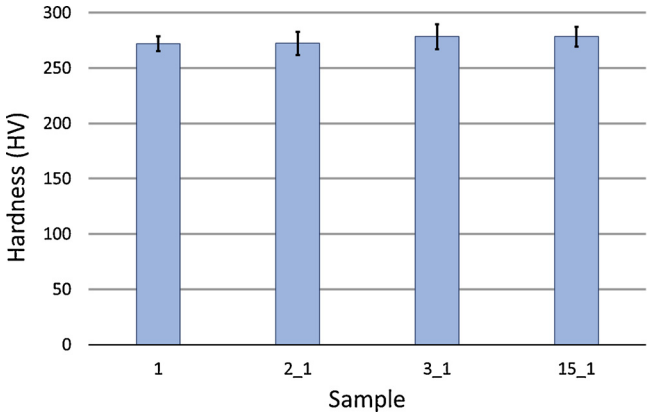

Fig. 4. Hardness measurements taken at the 1 st deposited layer of the samples, with varying number of total deposited layers in the single wall samples.

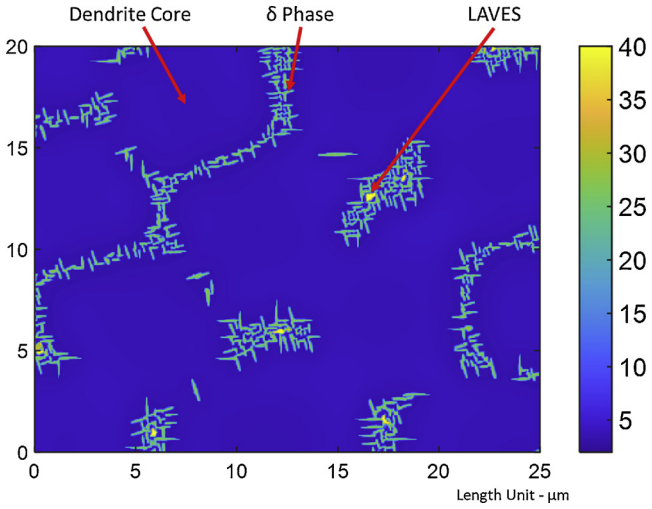

Fig. 5. Nb (wt%) distribution map after the solution heat-treatment simulation at 954 °C for 1 h using MICRESS.

Laves and eutectic γ nucleations, a critical undercooling value of 2 K was set. For simplicity of the simulation, only the liquid/γ interface was modelled as an anisotropic interface having cubic crystal anisotropy [25].

To investigate the effect of solution heat treatment on the microstructure of the LMPDED build, solution heat treatment simulation was performed. The microstructure predicted from the preceding thermal cycle simulation was used as the initial microstructure and the solution heat treatment simulation was carried out at 954 °C for 1 h (similar to the experimental solution heat treatment). During simulation, orthorhombic δ phase nucleation was allowed within the γ matrix. A critical undercooling of 1 K was set for the nucleation of the δ phase. The δ phase observed to have, $(010)_\delta \,||\, \{111\}_\gamma$; $[100]_\delta \,||\, <1\ \bar{1}\ 0>_\gamma$, relationship with γ matrix [26,27]. This relationship was used to set two different orientations for the δ phase in the simulation. Due to limitations in the anisotropic interface models in MICRESS, δ/ γ interface was modelled with a tetragonal anisotropy. Ageing heat treatment was not simulated since the current model resolution was not sufficient to model the precipitation of γ'/γ". A summary of the model parameters used is given in Table 3. Numerical parameters related to interfacial stiffness and mobility were chosen based on a trial-and-error approach, in order to get the correct morphology for the phases as observed in experimentally.

MICRESS simulations were performed on a Linux server equipped with AMD Opteron(tm) Processor 6386 SE - 2.8 GHz (16 cores, only 8 cores was used for the simulations) and 128 GB of RAM. Total simulation time took around 29 h.

3.3. CCT and TTT diagram calculation using JMatPro/Thermo-Calc

The time and temperature dependency of phase transformations during isothermal holding and continuous cooling can be represented by Time-Temperature-Transformation (TTT) diagrams and Continuous Cooling Transformation (CCT) diagrams respectively. They show the fraction of the phase transformation as a function of time and temperature. In order to investigate the effect of local elemental segregated on the precipitation of γ'/γ" and δ phases, TTT and CCT diagrams were generated using JMatPro (JMatPro is a trademark of Sun Microsystems, Inc - ver10.2) software. The local segregated elemental compositions predicted from the phase-field simulations were utilized for this purpose.

4. Results and discussion

In this section, most important experimental results from the microstructural observations relevant for the current modelling effort and their subsequent qualitative validation are discussed. More detailed information about the microstructural characterization of LMPDED Alloy 718 and the ensuing results are published elsewhere [28].

4.1. Effect of thermal cycling on the as-solidified microstructure

Fig. 1 shows the time-temperature history of the 1st layer of a 15-layer single wall deposited sample. Only measurement data related to the first 6-layers of the 15-layer deposition sample is being shown here. As can be seen from the figure, the 1st layer is subjected to multiple thermal cycles during deposition of multiple succeeding layers.

During solidification of Alloy 718, elements such as Nb, molybdenum (Mo) and Ti segregate into interdendritic region due to low solubility of these elements in the γ-matrix [4]. Such segregation of elements alters the local thermodynamics of Alloy 718 as well as the driving force for formation of various phases. Therefore, phases such as Laves, δ, NbC and TiN begin to form in the interdendritic region during solidification. In addition, segregation of these elements changes the precipitation kinetics of strengthening phases (γ'/γ") in the γ-matrix.

Fig. 2 shows the Nb distribution map after the 1st and 2nd cycles. During the 1st thermal cycle, the deposited melt material solidifies. As mentioned earlier, during solidification, Nb segregates into the interdendritic region. Nb is one of the elements that segregates most in Alloy 718. Therefore, its segregation can have a strong impact on the build microstructure [4,15,29]. The Nb distribution map reveals that the lowest concentration of Nb is found at the dendrite core, which represents the initial solidified part of the primary dendrite. When

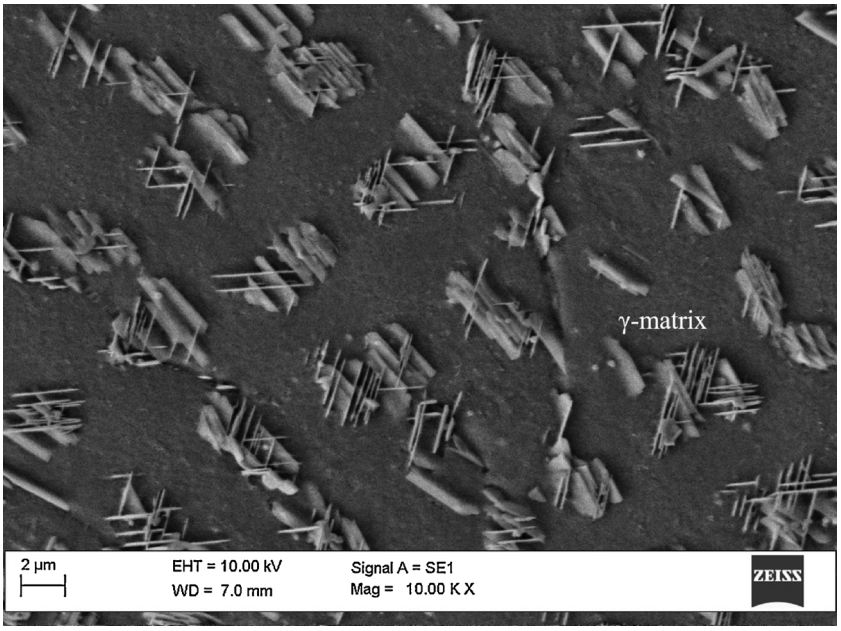

Fig. 6. Microstructure of the heat-treated 15-layer sample. Needle like precipitate in the γ-matrix are the δ precipitates. (SEM image was taken normal to the build direction at the 1 st deposited track of the 15-layer sample).

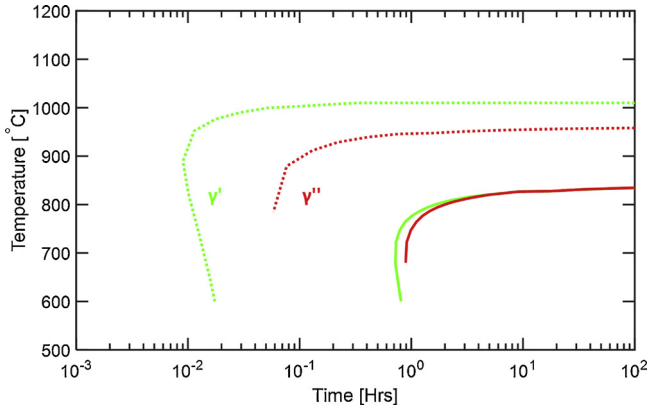

Fig. 7. Continuous cooling transformation (CCT) diagram created using segregated compositions predicted from MICRESS. Dotted line represent the 0.5% precipitation close to Laves phase and solid line represent 0.5% precipitation in the dendrite core.

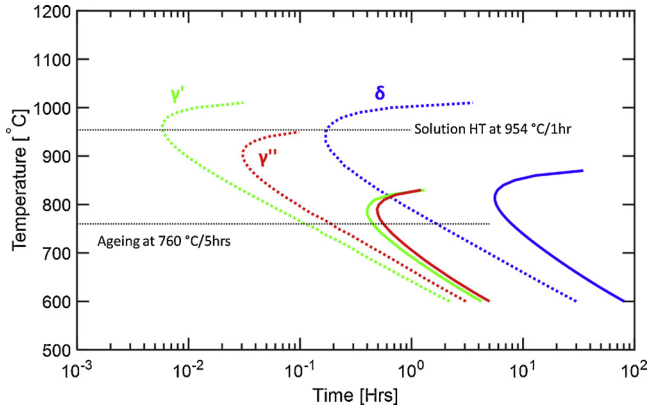

Fig. 8. Time temperature transformation (TTT) diagram created using segregated compositions predicted from MICRESS. Dotted line represent the 0.5% precipitation close to Laves phase and solid line represent 0.5% precipitation in the dendrite core.

moving away from the dendrite core to the interdendritic region, Nb concentration tends to increase. During the growth of the γ dendrite, Nb is continually rejected from the solid to the liquid. Hence, the Nb concentration in the liquid continues to increase. As a result, the liquid-solid interface advances into the liquid region with high Nb content, thereby resulting in an increase in Nb content from the dendrite core to the interdendritic region.

From the experimental work reported by Antonsson et.al. [29], it can be noted that the Nb content in the interdendritic liquid has to be above 20 wt% in order to form the Laves phase. During simulation, it was observed that the Laves phase starts to nucleate in regions where Nb content is greater than 17 wt%. This difference could be attributed to errors in the TCNI8 database or due to simplification of the alloy system. Formed Laves phase can be seen in Fig. 2 as bright yellow particles. The predicted Laves phase in the simulation contained ~40 wt% of Nb and ~0.9 wt% of Mo. These predicted values were higher and lower, respectively, compared to the values reported for Nb and Mo in the Laves phase [30–32]. One reason for higher Nb and lower Mo values in the predictions could be errors in the TCNI8 database. A simple Scheil simulation was performed using Thermo-Calc to check the Nb and Mo contents in Laves phase when it starts to form, and these were found to be around 41 wt% Nb and 0.7 wt% Mo. It was confirmed with the Thermo-Calc company that no parameter has been assessed for chromium (Cr)-Nb-Mo system in the TCNI8 database and this could have led to solubilities of Nb and Mo in Laves phase deviating from the expected values.

Fig. 2(b) shows the Nb distribution map at the end of the 2nd thermal cycle. It can be noted that there is almost no difference in the Nb distribution and the formed Laves phase at the end of the 1st and 2nd thermal cycles. One possible reason for this could be that, in the 2nd thermal cycle, the temperature in the 1st deposited layer was less than 1000 °C and, therefore, not high enough to have an impact on elemental diffusion and dissolution of the Laves phase. In addition, the time that the 1st deposited layer spent above 600 °C during the 2nd thermal cycle is ~2 s, which is too short to have any considerable impact on elemental diffusion in Alloy 718. Based on these observations, it can be expected that there will be negligible impact on elemental diffusion and Laves phase upon further thermal cycling (3rd, 4th,…). This is also corroborated by the experimentally measured Laves Phase + NbC area fraction measurements in the 1st deposited layer which revealed no

visible change with further deposition of layers (refer Fig. 3).

Fig. 4 shows the measured hardness values in the first layer in the LMPDED deposited samples. From the thermal measurements depicted in Fig. 1, it can be seen that during deposition of successive layers, the 1st deposited layer temperature goes through the γ'/γ" precipitation window for three consecutive thermal cycles. Hence, one can expect that the hardness in the 1st layer might progressively increase following deposition of the 2nd and 3rd layers. However, this was not clearly evident from the measured hardness values shown in Fig. 4. It is plausible that, even though the 1st deposited layer passes through the γ'/γ" precipitation window multiple times, the cumulative time that it spends within the precipitation window is inadequate to have a significant impact on the growth of γ'/γ" and, therefore, on the hardness values.

4.2. Effect of heat treatment on the as-built microstructure

Fig. 5 shows the Nb distribution map of the predicted microstructure after solution heat treatment (at 954 °C for 1 h) simulation. The needle-like phases that can be seen in the microstructure represent the δ phase. Some Laves phase particles can be seen in the microstructure even though a majority of them have dissolved. These δ needles (δ phase will look like needles in a 2D cross-section and have a platelet morphology in 3D) precipitate close to the Laves phase and in the interdendritic region of the as-built microstructure. One possible reason for this could be the change in the local driving force for precipitation of the δ phase in the above regions due to local segregated composition. Nb released during dissolution of the Laves phase also tends to diffuse to the surrounding interdendritic areas and aid growth of the δ phase. This observation is qualitatively in good agreement with the experimentally observed microstructure in a heat-treated 15-layer sample as shown in Fig. 6. with δ needles [28] observed mainly in the interdendritic region as predicted by the simulation. Rest of the samples (single layer, two layer and three layer) were also observed to have similar microstructures after the heat treatment.

4.3. Effect of element segregation on the precipitation kinetics

To ascertain the effect of elemental segregation on precipitation during the LMPDED process, CCT diagrams were created using JMatPro, taking the composition close to the Laves phase and in the dendritic core from phase-field simulations. As can be seen from Fig. 7, the kinetics of precipitation change due to changes in local composition. Close to the Laves phase, γ'/γ" precipitate earlier (more than an order of magnitude in time) compared to the core of the dendrite. Such accelerated kinetics could result in a higher number density of γ'/γ" close to Laves phase than in the core of the dendrite. This prediction is consistent with the experimental work performed by Segerstark et al. [28]. In the as-built microstructure, a higher number density of γ'/γ" was observed close to the Laves phase compared to the core of the dendrite.

Fig. 8 shows the TTT diagram generated based on the segregated element compositions at dendrite core and interdendritic regions. It can be clearly seen that there is a difference between the precipitation kinetics due to element segregation Close to Laves phase, the precipitation kinetics of γ'/γ" and δ are more than an order of magnitude faster compared to the dendrite core during the isothermal holding. In addition, as mentioned earlier, the Laves phase begins to dissolve during solution treatment at 954 °C, as seen from the heat treatment simulations. Hence, the Nb trapped in the Laves phase is released and diffuses to its surrounding. This favours growth of γ'/γ" and δ phases even further during solution heat treatment. During ageing heat treatment, γ'/γ" precipitates in the core of the dendrites also. However, the amount of these strengthening phases will be lower in the dendrite core as compared to the interdendritic region. In addition, growth of previously precipitated phases can also be expected.

5. Conclusions

In this study, microstructure evolution during laser metal powder directed energy deposition Alloy 718 and subsequent heat treatment have been investigated. For this purpose, phase-field modelling as well as precipitation kinetic modelling using JMatPro were utilised. The following conclusions were drawn based on the observed results:

- Phases such as Laves and γ'/γ" formed during deposition did not undergo any significant change during subsequent thermal cycles associated with deposition of subsequent layers
- Segregation of alloying elements in the interdendritic region was shown to change the precipitation kinetics of Alloy 718 and caused formation of high amounts of γ'/γ" compared to the dendritic core in the as-built condition
- The δ phase observed in the interdendritic region in heat-treated samples was precipitated during solution heat treatment at 954 °C for 1 h. This was predicted during the heat treatment simulation of the as-built microstructure. Elemental segregation was found to be responsible for this δ precipitation.
- A combined approach involving phase-field modelling and transformation kinetic modelling seems promising to provide better insight into microstructure formation during AM of Ni-based superalloys and subsequent heat treatments.

Acknowledgements

The authors would like to thank Dr. Bernd Böttger at Access e.V., Aachen, Germany for his valuable discussions and inputs regarding the modelling work in MICRESS. The funding from the European Regional Development Fund for project

3Dprint, and from KK Foundation (Stiftelsen för Kunskaps- och Kompetensutveckling) for project SUMAN-Next is also acknowledged.

References

[1] M.M. Attallah, R. Jennings, X. Wang, L.N. Carter, Additive manufacturing of Ni-based superalloys: the outstanding issues, MRS Bull. 41 (10) (2016) 758–764.
[2] C. Körner, Additive manufacturing of metallic components by selective electron beam melting—a review, Int. Mater. Rev. 61 (July (5)) (2016) 361–377.
[3] J.C. Lippold, S.D. Kiser, J.N. DuPont, Welding Metallurgy and Weldability of Nickel-Base Alloys, John Wiley & Sons, 2009.
[4] J.F. Radavich, The physical metallurgy of cast and wrought alloy 718, Superalloys 718 Metallurgy and Applications, (1989), pp. 229–240.
[5] ASTM F2792-12a, Standard Terminology for Additive Manufacturing Technologies (Withdrawn 2015), (2018).
[6] Ian Gibson, D. Rosen, B. Stucker, Additive Manufacturing Technologies 3D Printing, Rapid Prototyping, and Direct Digital Manufacturing, 2nd ed., Springer, US, 2014.
[7] Y. Tian, et al., Rationalization of microstructure heterogeneity in INCONEL 718 builds made by the direct laser additive manufacturing process, Metall. Mater. Trans. A 45 (September (10)) (2014) 4470–4483.
[8] T. DebRoy, et al., Additive manufacturing of metallic components – process, structure and properties, Prog. Mater. Sci. 92 (March) (2018) 112–224.
[9] F. Liu, et al., The effect of laser scanning path on microstructures and mechanical properties of laser solid formed nickel-base superalloy Inconel 718, J. Alloys Compd. 509 (March (13)) (2011) 4505–4509.
[10] H. Qi, M. Azer, A. Ritter, Studies of standard heat treatment effects on microstructure and mechanical properties of laser net shape manufactured INCONEL 718, Metall. Mater. Trans. A 40 (Oct ober (10)) (2009) 2410–2422.
[11] Y. Zhang, Z. Li, P. Nie, Y. Wu, Effect of cooling rate on the microstructure of laser-remelted INCONEL 718 coating, Metall. Mater. Trans. A 44 (December (12)) (2013) 5513–5521.
[12] Y. Zhang, Z. Li, P. Nie, Y. Wu, Effect of precipitation on the microhardness distribution of diode laser epitaxially deposited IN718 alloy coating, J. Mater. Sci. Technol. 29 (4) (2013) 349–352.
[13] X. Zhao, J. Chen, X. Lin, W. Huang, Study on microstructure and mechanical properties of laser rapid forming Inconel 718, Mater. Sci. Eng. A 478 (April (1–2)) (2008) 119–124.
[14] I. Tabernero, A. Lamikiz, S. Martínez, E. Ukar, J. Figueras, Evaluation of the mechanical properties of inconel 718 components built by laser cladding, Int. J. Mach. Tools Manuf. 51 (June (6)) (2011) 465–470.
[15] P. Nie, O.A. Ojo, Z. Li, Numerical modeling of microstructure evolution during laser additive manufacturing of a nickel-based superalloy, Acta Mater. 77 (September) (2014) 85–95.
[16] A. Segerstark, J. Andersson, L. Svensson, Evaluation of a temperature measurement

method developed for laser metal deposition, Sci. Technol. Weld. Join. 22 (January (1)) (2017) 1–6.
[17] M.L. Barron, Crack Growth-Based Predictive Methodology for the Maintenance of the Structural Integrity of Repaired and Nonrepaired Aging Engine Stationary Components, (1999).
[18] N. Moelans, B. Blanpain, P. Wollants, An introduction to phase-field modeling of microstructure evolution, Calphad Comput. Coupling Phase Diagrams Thermochem. 32 (2) (2008) 268–294.
[19] I. Steinbach, Phase-field models in materials science, Model. Simul. Mater. Sci. Eng. 17 (no. 7) (2009) 73001–73031.
[20] R. Acharya, J.A. Sharon, A. Staroselsky, Prediction of microstructure in laser powder bed fusion process, Acta Mater. 124 (February) (2017) 360–371.
[21] J. Eiken, B. Böttger, I. Steinbach, Multiphase-field approach for multicomponent alloys with extrapolation scheme for numerical application, Phys. Rev. E 73 (June (6)) (2006) p. 066122.
[22] B. Böttger, J. Eiken, M. Apel, Multi-ternary extrapolation scheme for efficient coupling of thermodynamic data to a multi-phase-field model, Comput. Mater. Sci. 108 (October) (2015) 283–292.
[23] Thermo-Calc Software, (2018) [Online]. Available: http://www.thermocalc.com/ . [Accessed: 25-May-2018]..
[24] G.A. Knorovsky, M.J. Cieslak, T.J. Headley, A.D. Romig, W.F. Hammetter, INCONEL 718: a solidification diagram, Metall. Trans. A 20 (October (10)) (1989) 2149–2158.
[25] Micress Group, MICRESS 6.4 - User Guide Volume II: Running MICRES, (2018).
[26] M. Sundararaman, N. Sachin, B.S. Jung, V. Amit, P. Bhaskar, R. Kishore, Evolution of δ phase microstructure in alloy 718, 7th Int. Symp. Superalloys 718 Deriv. (2010), pp. 737–750.
[27] M. Sundararaman, P. Mukhopadhyay, S. Banerjee, Precipitation of the delta-Ni3Nb phase in two nickel base superalloys, Metall. Trans. A 19 (3) (1988) 453–465.
[28] A. Segerstark, J. Andersson, L. Svensson, O. Ojo, Microstructural characterization of laser metal powder deposited alloy 718, Mater. Charact. 142 (June) (2018) 550–559.
[29] T. Antonsson, H. Fredriksson, The effect of cooling rate on the solidification of INCONEL 718, Metall. Mater. Trans. B 36 (February (1)) (2005) 85–96.
[30] M.M. Kirka, K.A. Unocic, N. Raghavan, F. Medina, R.R. Dehoff, S.S. Babu, Microstructure development in electron beam-melted inconel 718 and associated tensile properties, JOM 68 (March (3)) (2016) 1012–1020.
[31] K. Sivaprasad, S. Ganesh Sundara Raman, Influence of weld cooling rate on microstructure and mechanical properties of alloy 718 weldments, Metall. Mater. Trans. A 39 (September (9)) (2008) 2115–2127.
[32] J.J. Schirra, R.H. Caless, R.W. Hatala, The effect of laves phase on the mechanical properties of wrought and cast + HIP inconel 718, Superalloys 718, 625 and Various Derivatives (1991), (1991), pp. 375–388.
[33] J. Kundin, L. Mushongera, H. Emmerich, Phase-field modeling of microstructure formation during rapid solidification in inconel 718 superalloy, Acta Mater. 95 (August) (2015) 343–356.
[34] N. Zhou, et al., Computer simulation of phase transformation and plastic deformation in IN718 superalloy: microstructural evolution during precipitation, Acta Mater. 65 (February) (2014) 270–286.